Supporting Information: Surface Forces and Structure in a Water-in-Salt Electrolyte

Timothy S. Groves,[†] Carla S. Perez-Martinez,[‡] Romain Lhermerout,[¶] and Susan Perkin[*,†]

[†]*Physical and Theoretical Chemistry Laboratory, University of Oxford, Oxford, UK*

[‡]*London Centre for Nanotechnology, University College London, London, UK*

[¶]*Laboratoire Charles Coulomb, Université de Montpellier, CNRS, Montpellier, France*

E-mail: susan.perkin@chem.ox.ac.uk

Experimental Details

Experiments are performed using a surface force balance, SFB. Further details on the preparation of the SFB for measurement, mechanical components, optical set-up, and analysis of data are given here. A schematic of the interior of the SFB is shown in Figure S1.

Surface Preparation

The surfaces used in the SFB consist of single facet mica pieces of uniform thickness prepared in advance of the measurement. Muscovite mica is cleaved by hand in a laminar flow hood, LFH, to prevent the occurrence of particles on the mica surface. Large, thin, single-faceted pieces of mica (up to 10 cm^2 area with thickness 1-10 μm) are cleaved, cut using a hot platinum wire, and adhered to a larger, freshly cleaved, thick sheet of mica, referred to as a

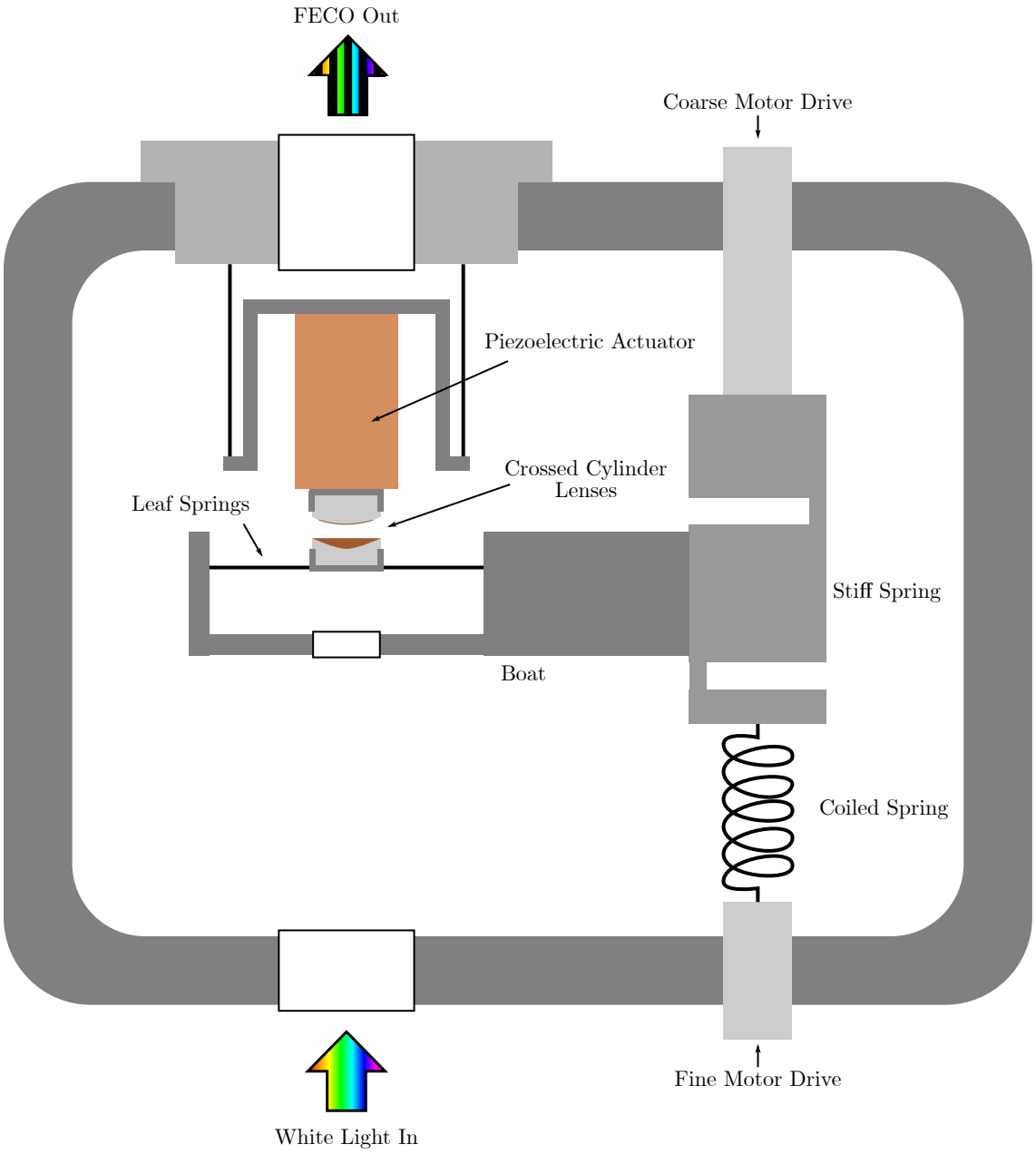

Figure S1: The interior of the SFB used in this work. Lenses are mounted in a crossed cylinder configuration. The lower lens may be moved using either the coarse or fine motor drive, while the upper lens may be moved using the piezoelectric actuator. White light enters through a window at the bottom of the chamber, is incident on the lenses, and the emerging interference pattern exits through a window at the top of the chamber as shown.

base sheet. This method has previously been shown to produce clean pieces of mica for SFB measurements.[S1] Multiple single faceted thin pieces of mica are placed on the base sheet. Cleaving for a single base sheet takes place over a maximum of two hours. After this time, adsorbates are likely to have contaminated the exposed portions of the base sheet, and no further thin pieces may be placed on the base sheet. Base sheets are then placed under high vacuum ($\sim$ 10^{-6} mbar) and a thin layer of silver is evaporated onto them, coating the exposed side of the thin mica pieces with a silver mirror. Silvered mica is stored in a desiccator under vacuum.

Prior to an experiment, cylindrical silica lenses with $R \approx 10$ mm are heated to 180°C. A thin, smooth coat of epoxy resin (EPON 1004, Shell Chemicals) is then applied to the lens. The silvered mica is taken and cut into pieces with area $\approx$ 1 cm. The cut pieces of mica are lifted from the base sheet and placed, silver side down, on the lens such that the apex of the lens is covered by mica. Capillary action within the glue pulls the mica down over the lens, presenting a smooth, clean cylindrical surface with radius of curvature $R \approx 10$ mm. Once this has taken place, the lens is removed from the heat and allowed to cool before being mounted in the SFB chamber in the crossed cylinder configuration shown in Figure S1 and Figure 1 of the main text.

Mechanical Components

The lower lens is mounted within a boat. The boat, shown in Figure S1, is an open-topped stainless steel container that can be filled with liquid if required. Within the boat, the lens socket is suspended on a set of leaf springs, whose spring constant k_N is calibrated prior to an experiment by measuring the deflection of the leaf springs under a series of 'dummy lenses' of known mass. For all experiments conducted in this work, $k_N \approx 125$ N m^{-1}. The boat is mounted on a slide connected directly to a stepper motor. Termed the coarse motor, this motor allows motion over a range of a few centimetres, with a micrometric precision. The slide is separated from a second, identical stepper motor by a differential spring mechanism.

The spring mechanism, consisting of a coiled and stiff spring and shown in Figure S1, damps vibrations from the second motor and reduces the motion by a factor of around 1000. Termed the fine motor, this motor allows motion over a range of a few tens of micrometers, with a nanometric precision. The upper lens mount sits within a piezoelectric actuator that allows for vertical motion over a range of around 1 micrometer with precision below 0.1 nanometer.

Optical Details

Collimated white light from an Ar-Xe arc lamp source (Osram) is incident on the two lenses as shown in Figure 1 of the main text. The transmitted light is focused onto a spectrometer grating and emerges as a series of Fringes of Equal Chromatic Order, FECO. A formal mathematical treatment of the FECO has been undertaken[S2,S3] and refined for use in SFB.[S4] Examples of FECO recorded in this work are shown in figure S2. Owing to the birefringent nature of the mica, fringes appear as a series of doublets. Two orders of fringes can be seen: those with negative curvature are odd fringes while those with only positive curvature are even fringes. A fringe with odd order is chosen and labelled as the p *fringe* (the leftmost fringe in figure S2). All other fringes are labelled relative to the p fringe. Figure S2 shows p, $p-1$ and $p-2$ fringes.

Surfaces are first brought into contact in air using the piezoelectric actuator, where strong adhesion between the fresh mica surfaces leads to a flattening of the fringes (top image of figure S2). From this contact image, and by comparison with known mercury green and yellow lines, the wavelength of the p and $p-1$ fringes at contact (with no film between the surfaces) can be calibrated and from this the mica thickness can be calculated. Figure S2 shows fringes with 3.36 μm mica. A secondary fringe, an area of high light intensity centred on the $p-1$ fringe, can be seen.

The surfaces are separated and a droplet of liquid is injected between the lenses (note that the boat can be filled with the fluid of interest where necessary). The surfaces are brought back into contact (bottom image of figure S2). The thin liquid film confined between the

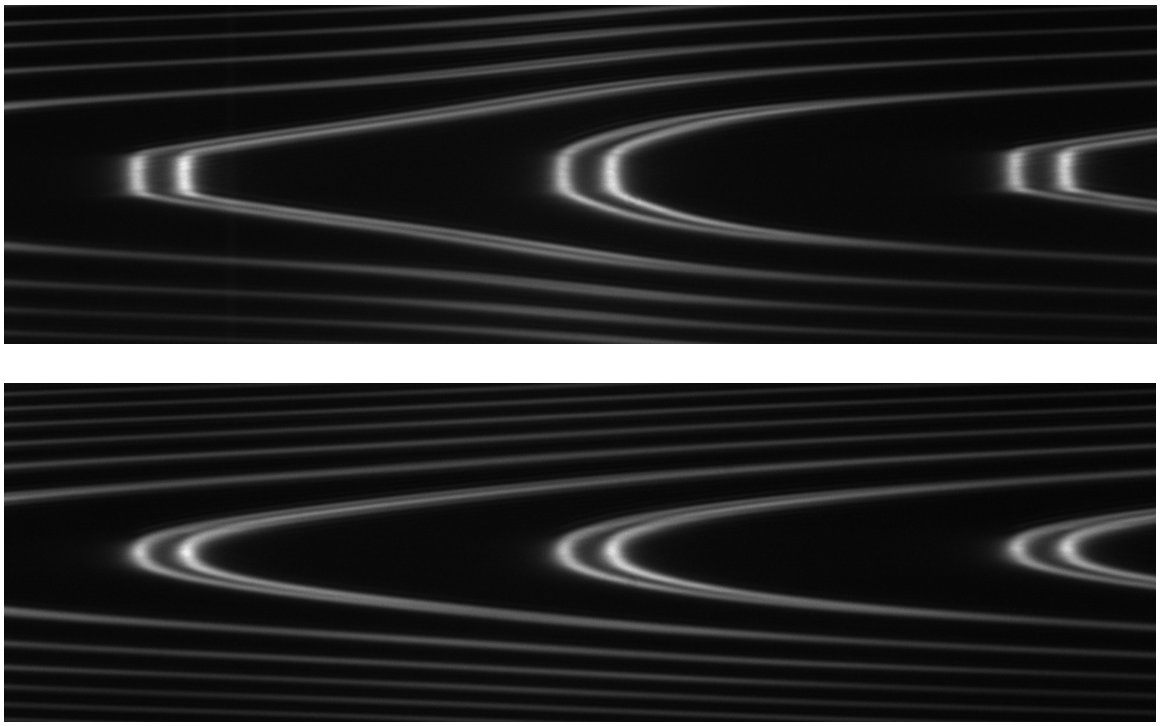

Figure S2: Examples of FECO captured in this work. The x dimension shows wavelength, increasing left to right, while the y dimension shows position on the mica surfaces with the apices of the fringes corresponding to the point of closest approach between the crossed cylinders. *Top:* FECO at surface contact in air, showing characteristic flattening arising from deformations within the epoxy glue (outside of the interferometer) under strong adhesive forces. *Bottom:* FECO at surface contact across a liquid film. In each case, the leftmost fringe is labelled the p fringe and subsequent fringes are labelled with respect to the p fringe.

lenses reduces the adhesion between the mica surfaces, preventing flattening, while the large liquid refractive index (compared to the refractive index of air) masks the secondary fringes. By considering the geometry of the p fringe at this position, the local radius of the contact spot can be calculated. Figure S2 shows a spot with radius 9.4 mm.

The surfaces are separated to a small distance using either the piezoelectric actuator or the fine motor, and the evolution of the fringes is tracked using a CCD camera with image frequency ≈ 5 Hz. By comparing the wavelengths of the p and $p-1$ fringes, λ_p and λ_{p-1} to the contact wavelength of the p fringe, $\lambda_{p,\ D=0}$, the separation of the surfaces, D, can be calculated:

$$\tan(k\mu_{\text{medium}}D) = \frac{2\overline{\mu}\sin\theta}{(1+\overline{\mu}^2)\cos\theta \pm (\overline{\mu}^2-1)} \tag{1}$$

where k is the wavenumber of the light, $k = 2\pi/\lambda$,

$$\bar{\mu} = \frac{\mu_{\text{mica}}}{\mu_{\text{medium}}}, \quad \theta = \frac{p\pi(\lambda_p - \lambda_{p,\ D=0})}{\lambda_p}, \quad p = \frac{\lambda_{p-1,\ D=0}}{\lambda_{p-1,\ D=0} - \lambda_{p,\ D=0}}$$

and μ_k is the refractive index of component k. The refractive indices of solutions of LiTFSI have been measured using an Abbe 60 refractometer (Bellingham and Stanley), and are shown with concentration in table S1.

Table S1: The refractive indices of LiTFSI solutions of varying concentration.

Molality / mol kg^{-1}	Refractive index	Temperature / ^{o}C
4.7	1.3562	24.2
8.1	1.3621	22.6
12.2	1.3694	21.3
13.5	1.3668	23.6

Overall, this technique allows surface separation to be measured with a precision of ≈ 0.02 nm, given by the RMS noise of the signal (relevant when comparing distances within a single experimental run and between runs on the same measurement spot where no change to the optical path has taken place), and an accuracy of ≈ 1 nm (relevant when comparing

between different measurement spots and different experiments), as changes in the optical path can lead to small variations in the absolute distance measurement.

Measurement Details

Each experiment consists of a series of experimental runs during which the surfaces are moved together and apart. Each run probes part of the total force profile. By combining multiple runs that probe different parts of the force profile, the total force profile can be resolved. Runs are made using the fine motor when large forces are required, for example when the inner layers are probed or adhesive forces are measured, or using the piezoelectric actuator when smaller forces of outer layers and long distance forces are measured. Illustration of the analysis process is shown in this section,with all data taken from a single experiment performed on an 11.64 m aqueous LiTFSI solution, however the process for analysing data is the same for all measurements reported.

As the fine motor has a much larger range of displacement, it can apply substantially more force, and as such is used to investigate the force barriers and adhesive wells of the structural force. An example of a run collected using the fine motor is shown in figure S3 and figure S4.

From these force profiles an oscillatory wavelength can be obtained. The positions of jump-out from each adhesive well are measured, and plotted against the index of the layer, as shown in S5. Applying a linear fit to the resulting line gives the oscillatory wavelength, λ_o.

One disadvantage of the fine motor is that the mechanical motion tends to impart additional noise into the system which can obscure small magnitude forces such as underscreening. For this reason, the smaller forces that dominate the force profile at greater separations are measured using a piezoelectric actuator, which imparts no such vibrations. An example of a run collected using the piezoelectric actuator is shown in figure S6, which clearly highlights the existence of a weak, long-range exponentially decaying force.

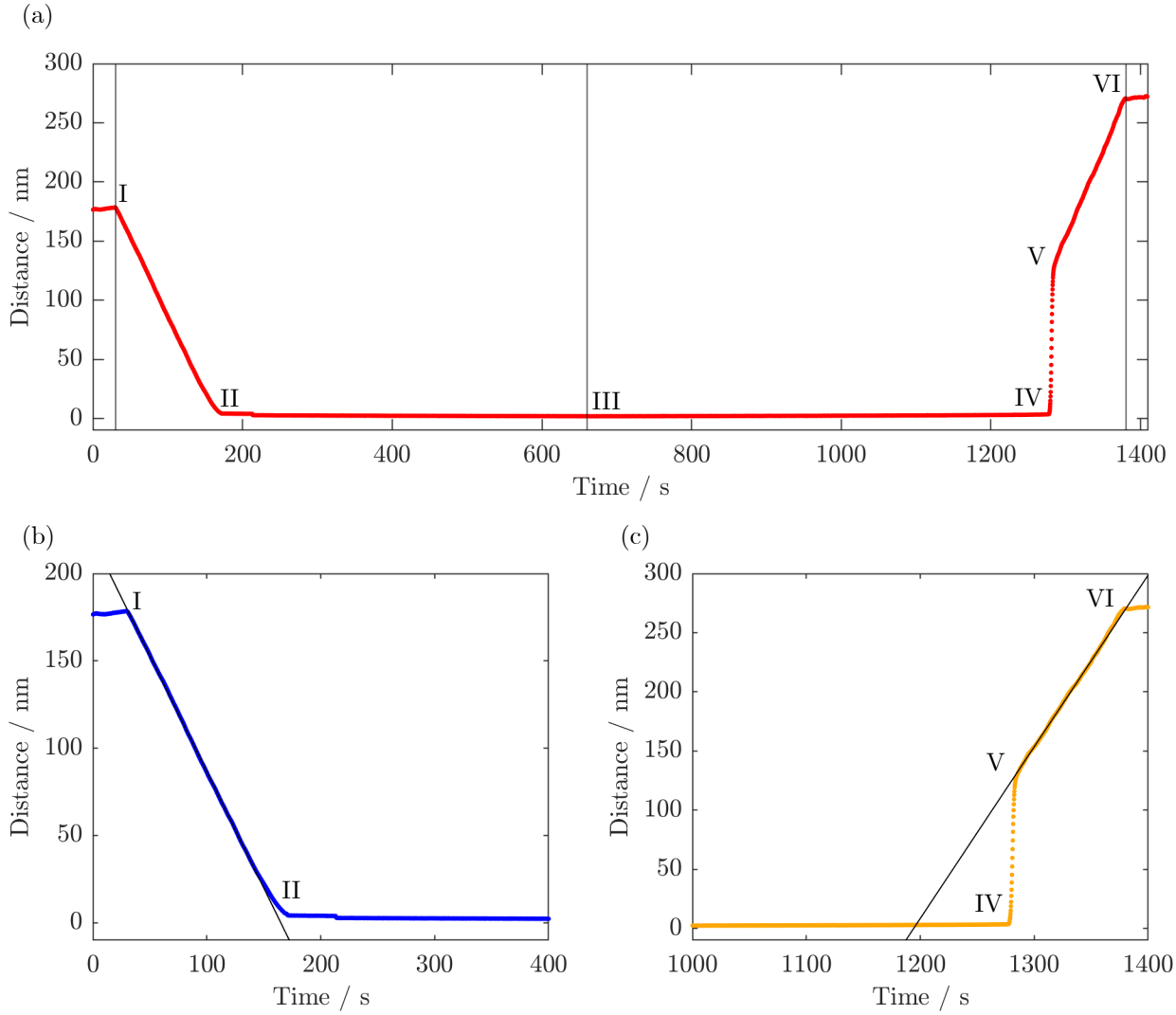

Figure S3: The analysis process for a fine motor force profile. (a): The total distance vs time for a single fine motor run measuring normal forces on approach to and retraction from layer $i = 2$, with distances calculated using equation 1. (b): The approach part of the run showing the linear baseline, giving a velocity of 1.33 nm s^{-1}. At contact, points to the right of the baseline indicate a repulsive force. (c): The retraction part of the run showing the linear baseline, giving a velocity of 1.45 nm s^{-1}. Points to the right of the baseline indicate an attractive, adhesive force. I: The approach is begun. II: Surface contact is reached and the layering regime resolved. III: The approach is stopped and the retraction is begun. IV-V: The surfaces jump out of adhesive contact. VI: The retraction is stopped.

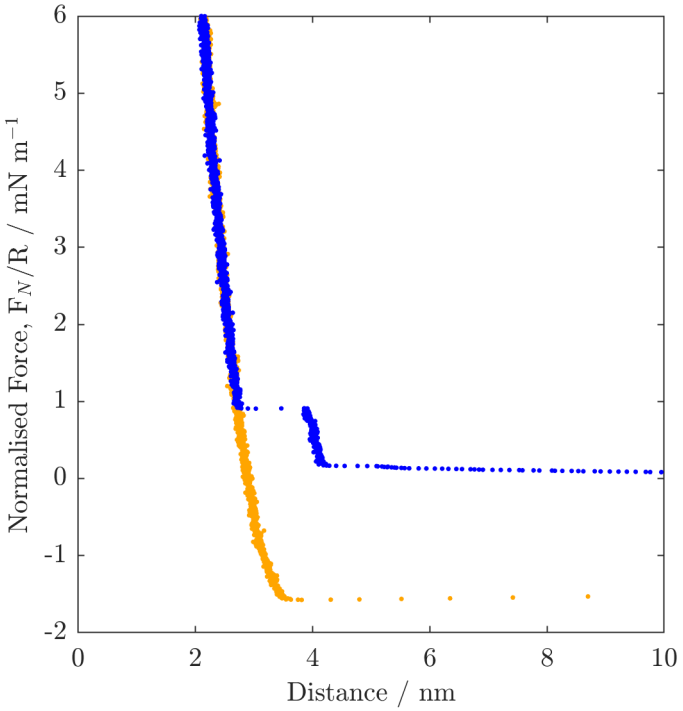

Figure S4: The force profile resulting from the run shown in figure S3. Points measured on approach are shown in blue and those measured on retraction are shown in yellow. Outer layers $i = 4$, 3 and 2 are observed on approach, and the adhesive well of layer $i = 2$ is measured on retraction.

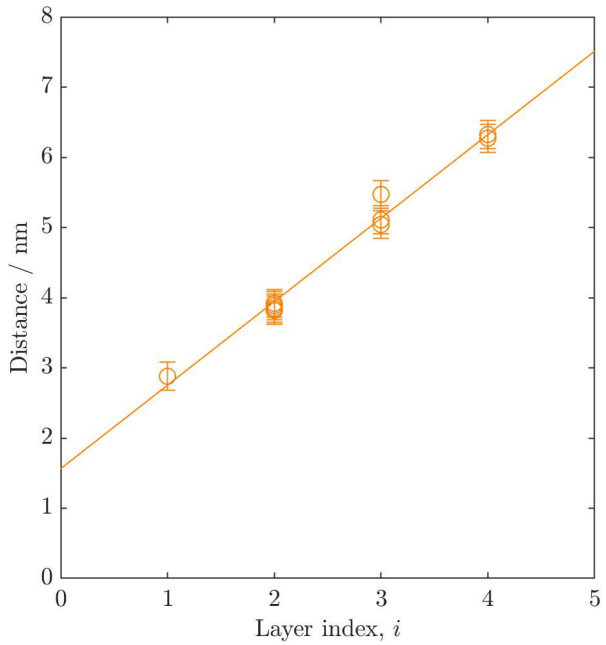

Figure S5: A linear fit of jump out position against layering index for an 11.64 m aqueous LiTFSI solution. The layering wavelength in this case is found to be 1.2 ± 0.1 nm.

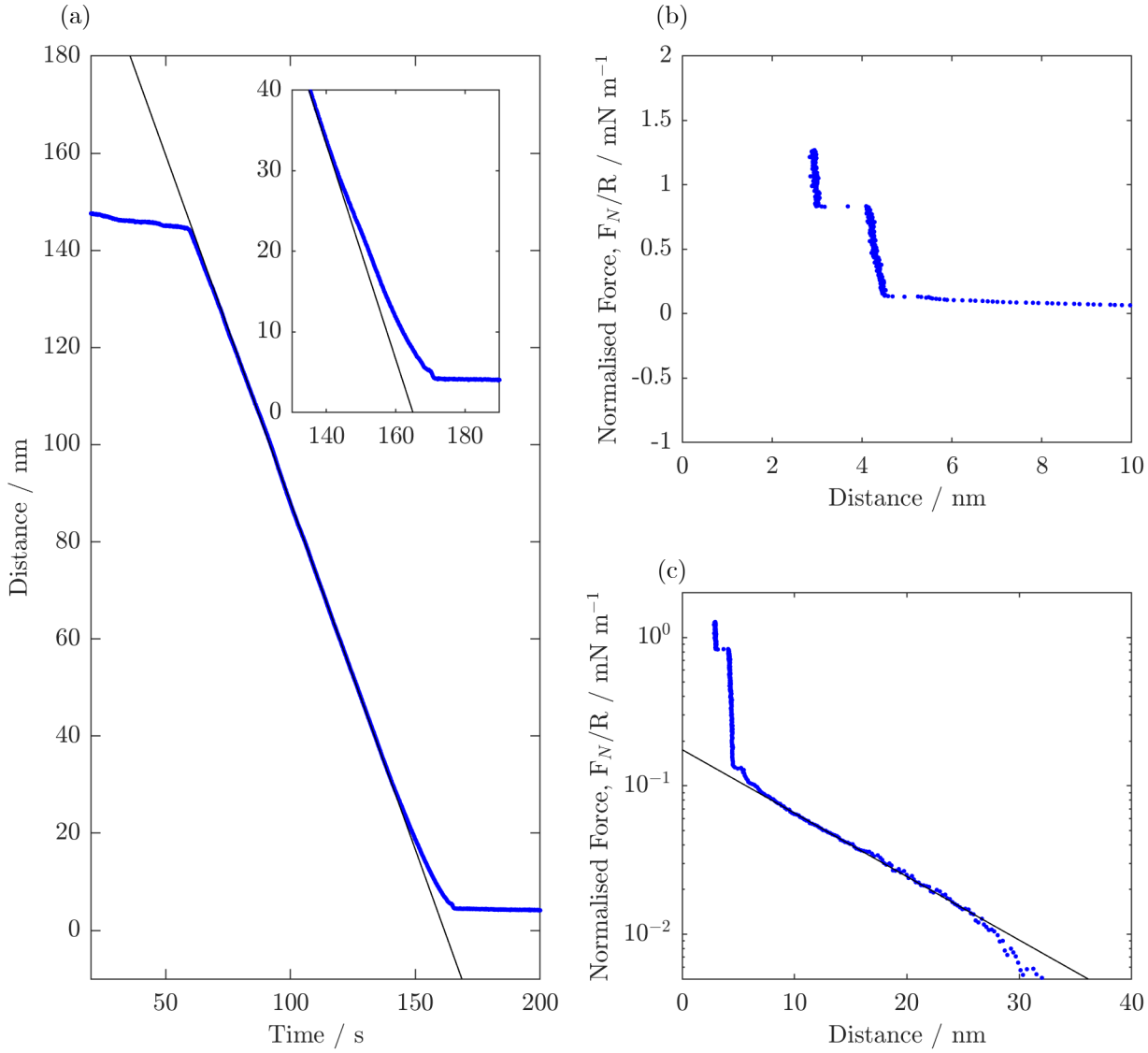

Figure S6: The analysis process for a piezoelectric actuator force profile. (a): The distance vs time for the approach showing the linear baseline, giving a velocity of 1.43 nm s^{-1}. The inset shows a long range repulsive force extending to around 30 nm surface separation. (b): The normal forces plotted on a linear scale. (c): The normal forces plotted on a logarithmic scale. This shows clearly the existence of the three outer layers as well as an exponentially decaying monotonic repulsive force with decay length 10.2 nm.

Over the course of a measurement, several tens of runs are carried out over a range of velocities and contact spots using both the fine motor and the piezoelectric actuator to provide the motion. The total measured forces are shown on a linear scale in Figure S7, highlighting the high precision and accuracy of this measurement method. The forces are shown on a logarithmic scale in Figure S8, which highlights the drifts that can occur at low velocities and using the fine motor.

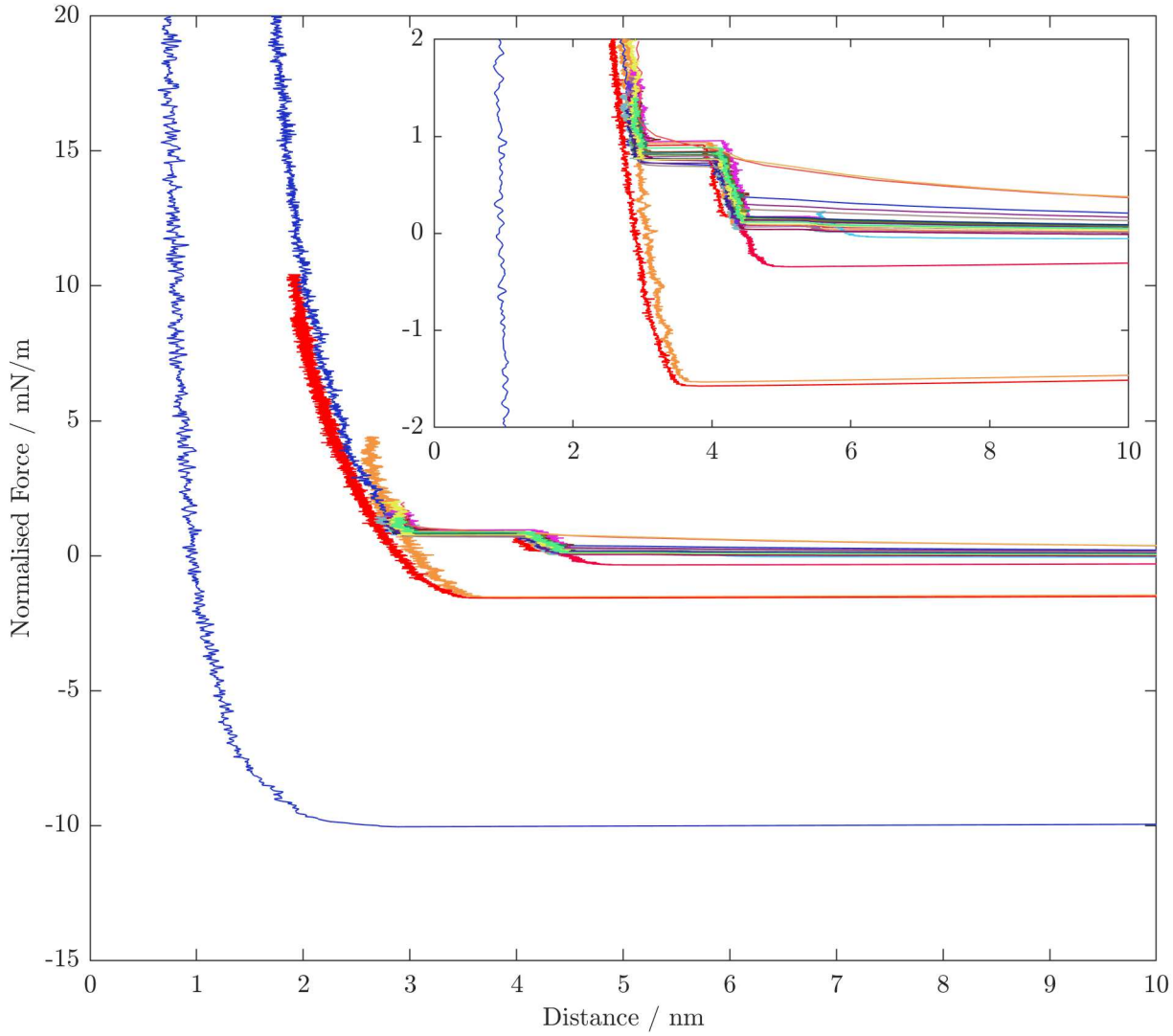

Figure S7: Force profiles of all runs collected for a single measurement spot, plotted on a linear force scale. Each run is shown in a different colour. The inset shows the same plot over a smaller range of forces. The close overlap of runs highlights the high precision and accuracy of this technique.

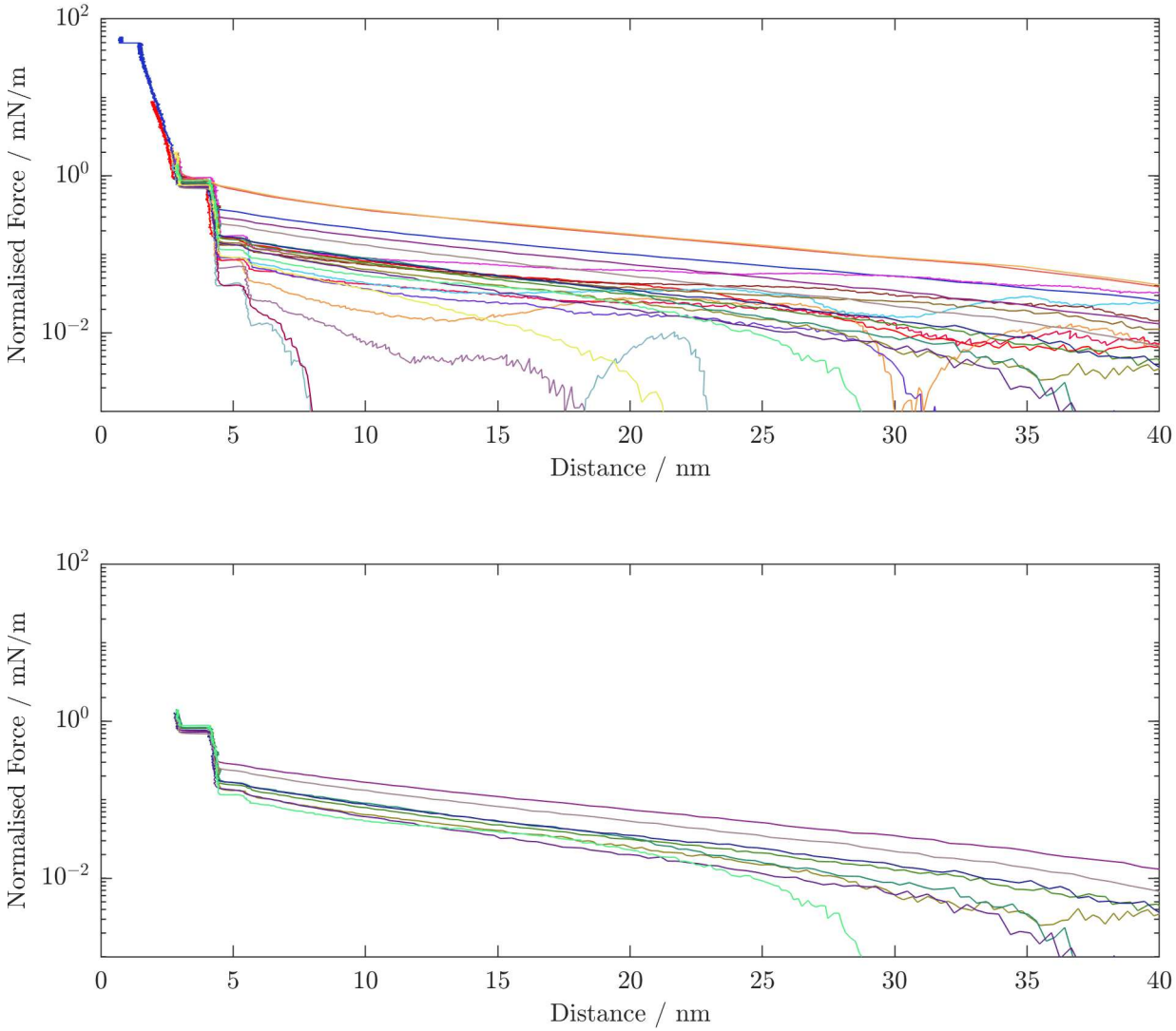

Figure S8: All forces plotted on a logarithmic scale. *Top:* Each force profile is shown. Many show substantial drift, either arising from vibrations within the system (e.g. from the fine motor) or from random thermal fluctuations that occur during the run. *Bottom:* Only force profiles with clean decays to ≈ 30 nm are shown. These tend to not be too slow, where thermal drifts can distort approaches, or too fast, where hydrodynamic forces can be significant.

Underscreening lengths are measured by fitting the logarithmic forces shown in Figure S8 to a linear baseline close to contact. Hydrodynamic forces were not relevant in these measurements due to the low viscosities of the solutions and the low approach velocities, however their contribution has been carefully analysed in a recent work.[S5]

In order to plot figure 2 of the main text, runs with minimal drift, each probing different parts of the force profile are chosen. They are then shifted by ≤ 0.5 nm to align with the first run on the first contact spot of that measurement, and non-equilibrium points recorded during dynamic processes (adhesive jump-outs or layering transitions) are removed in order to show only equilibrium forces for clarity.

References

(S1) Perkin, S.; Chai, L.; Kampf, N.; Raviv, U.; Briscoe, W.; Dunlop, I.; Titmuss, S.; Seo, M.; Kumacheva, E.; Klein, J. Forces between Mica Surfaces, Prepared in Different Ways, Across Aqueous and Nonaqueous Liquids Confined to Molecularly Thin Films. *Langmuir* **2006**, *22*, 6142–6152.

(S2) Tolansky, S. *Multiple-Beam Interferometry of Surfaces and Films*; Oxford University Press, 1949.

(S3) Tolansky, S. *An Introduction to Interferometry*; Longmans, Green and Co LTD, 1955.

(S4) Israelachvili, J. N. Thin film studies using multiple-beam interferometry. *Journal of Colloid and Interface Science* **1973**, *44*, 259–272.

(S5) Lhermerout, R.; Perkin, S. Nanoconfined ionic liquids: Disentangling electrostatic and viscous forces. *Phys. Rev. Fluids* **2018**, *3*, 014201.